Progress In Electromagnetics Research B, Vol. 117, 29–42, 2026

(Received 19 November 2025, Accepted 24 December 2025, Scheduled 21 January 2026)

Adapting Operational Volume Scanning to Low-Power FMCW: System Development and Physically-Informed ML Calibration

Asif Awaludin[1, 2, *], Dwiyanto[3], Rahmat Triyono[5], Yunus S. Swarinoto[5], Erwin Makmur[5],
Beno K. Pradekso[6], Oktanto Dedi Winarko[6], Muhammad F. A. Maggaukang[6], Liarto[7],
Donaldi S. Permana[5], Roni Kurniawan[5], Rezky Yunita[5], Mohamad H. Nurrahmat[5],
Thahir D. F. Hutapea[5], Agung Majid[5], Muhamad R. Taufik[5], Warjono[5], Ferdinandus E. Penalun[5],
Bobby Harnawan[6], Doddy D. Patriadi[6], Muhamad R. Anggara[6], Hastuadi Harsa[4], Alfan S. Praja[2],
Fatkhuroyan[5], Wido Hanggoro[5], Muhammad N. Habibie[5], Welly Fitria[5], Rahayu S. S. Sudewi[5],
Asteria S. Handayani[5], Sri Noviati[5], and Vestiana Aza[5]

[1] *Computer Engineering Department, School of Electrical Engineering*
Telkom University, Jl Telekomunikasi 1, Bandung Regency, West Java 40257, Indonesia
[2] *Research Center for Climate and Atmosphere, National Research and Innovation Agency*
Jl Raya Puspiptek 60, Tangerang Selatan, Banten 15310, Indonesia
[3] *Research Center for Satellite Technology, National Research and Innovation Agency*
Jl Cagak Satelit No. 8, Kabupaten Bogor, Jawa Barat 16310, Indonesia
[4] *Research Center for Geoinformatics, National Research and Innovation Agency*
Jl. Sangkuriang, Bandung, Jawa Barat 40135, Indonesia
[5] *Agency for Meteorology Climatology and Geophysics, Jl Angkasa I No. 2, Jakarta Pusat, Jakarta 10720, Indonesia*
[6] *PT. Dua Empat Tujuh, Jl Prof. Dr. Satrio KAV 6, Jakarta Selatan, Jakarta 12940, Indonesia*
[7] *PT. Sapta Cakra Manunggal, Sorogenan II, Sleman, Yogyakarta 12940, Indonesia*

ABSTRACT: This study presents the development and evaluation of a transportable X-band frequency-modulated continuous-wave (FMCW) weather radar (WR) that successfully adapts operational volumetric scanning strategies typically reserved for high-power to low-power pulsed systems. The radar integrates a complete radio-frequency chain, a carbon graphite antenna, and a dedicated real-time processing unit designed for operational volumetric scanning. It performs rapid 4-minute volume scans across seven elevation angles (0.00°–15.88°) with nonuniform spacing optimized for low-level atmospheric sampling, while a 2 RPM rotation provides full azimuthal coverage every 30 s. The resulting Column Maximum (CMAX) product synthesizes reflectivity from all elevation angles to depict a three-dimensional precipitation structure, demonstrating a spatial observational capability distinct from traditional profiling FMCW radars. A three-stage hierarchical physically-informed architecture calibration framework was implemented to ensure quantitative accuracy in the FMCW WR's measurements, using collocated C-band Doppler Weather Radar (CDWR) observations as reference data. Validation through internal five-fold Group K-Fold cross-validation, Leave-One-Pair-Out (LOPO) testing, and external evaluation using independent radar pairs demonstrated the framework's robustness. The case study of localized urban convection observed by the FMCW WR shows that the developed low-cost radar offers much finer range resolution and can reveal detailed structures within convective cells.

1. INTRODUCTION

FMCW radar has several advantages over pulse radar. It provides higher range resolution (as good as 0.5 meters) and better measurement accuracy (down to micrometers for some sensors). FMCW radar uses lower peak power, so it consumes less energy and emits less electromagnetic radiation, which makes antenna placement easier [1]. It works reliably in all weather conditions, including rain, humidity, fog, and dust, and is unaffected by temperature or heat. Unlike Doppler radars, it can track motion across surfaces and measure both distance and speed at the same time without needing extra antennas or pulses [2].

Weather radar uses pencil-beam antennas for precise precipitation scanning. The most common types are slotted waveguide array antennas [3, 4] and parabolic dish antennas [5]. In slotted waveguide antennas, the slot's length and direction set the frequency and polarization, while the number of slots affects the gain [6, 7]. In parabolic dish antennas, feedhorn sets the frequency and polarization, and the reflector increases the gain [8]. Weather radars use rotators for azimuth and elevation to scan large volumes or to follow custom scanning patterns.

X-band weather radar scanning methods vary depending on the speed, coverage, and purpose. Most pulsed radar systems use volume scanning as a standard. For example, the MP-X radar [9] completes an 11-elevation scan in about 3 minutes for detailed 3D images of storms. The BoXPol radar [10] finishes a 10-elevation scan in 5 minutes, balancing detail and practicality for regular weather monitoring [11]. The RaXPol radar [2] is designed for fast-changing weather and completes a full scan in just 20 seconds, which is useful for tracking short-lived events

---

[*] Corresponding author: Asif Awaludin (asifaw@telkomuniversity.ac.id).

doi:10.2528/PIERB25111901

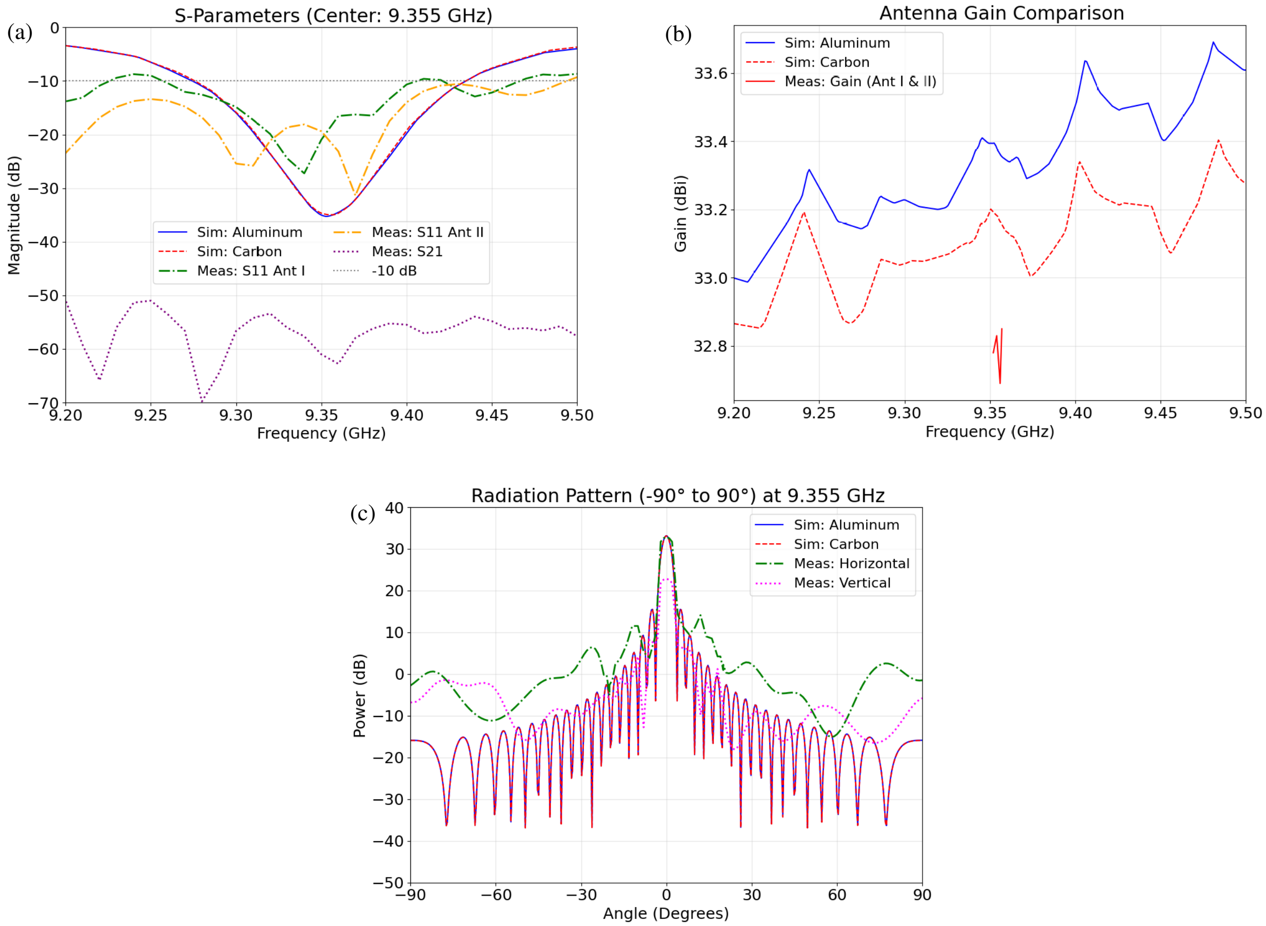

FIGURE 1. Simulated parameters of the dish antenna using aluminum and carbon graphite materials. The measured parameters are from a dish antenna using carbon graphite only. (a) Return loss, (b) gain, and (c) radiation pattern.

like tornadoes. By comparison, FMCW radar systems typically focus on vertical profiles or fixed directions. The FMCW Integrated Doppler Radar Array (IDRA) [12] is built to study the drizzle and lower atmosphere, mostly using a fixed low angle to monitor near-surface rain. As a result, while pulsed radars often use volume scanning, this method is rarely used for smaller FMCW radars.

Calibrating FMCW radar reflectivity for scanning systems is difficult because accurately measuring the radar constant is challenging. This constant depends on factors like power, antenna gain, and system losses, all of which can change with temperature [13, 14]. As a result, calibration needs to account for temperature and range, so one-time calibration is not enough. Usually, calibration uses metal targets placed far from the radar to make sure the beam is formed correctly [14, 15]. For high-frequency radars, this distance can be hundreds of meters, making it challenging to position the targets for all scan angles. Using metal spheres or corner reflectors provides a known signal, but this process is slow and only checks a few points [16].

This research addresses this gap by introducing a portable X-band FMCW radar for volumetric scanning. The main innovation is the full integration of a specialized RF chain with a custom transmitter, sensitive receiver, and carbon graphite antenna to mimic the multi-elevation scanning of powerful systems but with lower power. It also includes a fast signal-processing unit for quick, real-time data collection and results.

This research also addresses a critical gap in the operational deployment of high-resolution atmospheric sensing by developing a novel (machine learning (ML)-based framework for volume-scanning reflectivity calibration of FMCW WR systems. The principal innovation of this study lies in introducing a three-stage, physically-informed ML (PIML) calibration architecture that uniquely couples inherent radar characteristics with advanced data-driven learning. Unlike conventional static calibration methods or simple statistical adjustments, this framework offers a dynamic, adaptive, and highly granular solution, which is essential for volume-scanning consistency.

2. DEVELOPMENT AND CALIBRATION METHODS

2.1. Antenna System and Radome for Volume Scanning

The system employs a co-located pair of identical parabolic dish antennas for both transmission and reception. The reflector antenna has a dish diameter of 600 mm operating at a center frequency of 9355 MHz. We performed Finite-Difference Time-Domain (FDTD) simulations using aluminum and carbon graphite as antenna reflector materials, yielding maximum gains of 33.26 dBi and 33.04 dBi at 9355 MHz, respectively

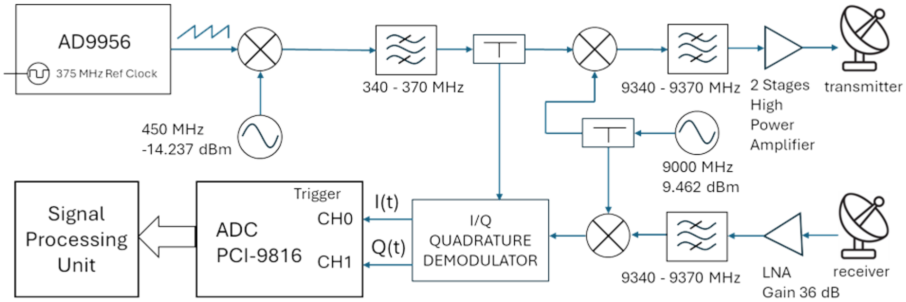

FIGURE 2. The schematic diagram of the developed FMCW radar consists of the transmitter and receiver parts.

(Fig. 1(b)). These results demonstrate that aluminum's superior conductivity results in a slightly higher gain than carbon graphite, but carbon graphite offers lighter weight and non-corrosive properties.

Highly conductive materials, like metals, generate strong reflected waves owing to the surface currents. In contrast, carbon graphite conductive paints have lower conductivity and often contain non-conductive binders, resulting in reduced reflective properties [17]. For instance, an 85% graphite and 15% carbon black mix has a resistivity of about 0.037 Ω·m, while a 2.6:1 ratio lowers it to 0.029 Ω·cm (0.00029 Ω·m). Graphite paints are used for shielding against electromagnetic and radio frequency interference, although their resistivity is significantly higher than that of metals like copper, which is approximately 1.68×10^{-8} Ω·m.

The fabricated antenna was characterized using a Vector Network Analyzer up to 14 GHz. It operates within a frequency band of 9.3 GHz to 9.4 GHz, with a measured isolation of −62 dB at 9.355 GHz, as illustrated in Fig. 1(a). The radiation pattern and gain measurements showed a peak gain of 32.8 dBi in the E-plane and 22.8 dBi in the H-plane. Both planes exhibited a 3-dB beamwidth of approximately 4 degrees at 9.355 GHz, as depicted in Fig. 1(c). The carbon graphite coating achieved a gain of 32.8 dBi at 0° in the E-plane, just 0.24 dBi below the 33.04 dBi simulated gain of a carbon graphite antenna, demonstrating strong performance.

TABLE 1. Specification of transmitter and receiver systems.

Parameter	Specification
Operating Frequency	9355 MHz with 5 MHz BW
Carrier Frequency Signal	9000 MHz, 9.462 dBm
Type Signal	FMCW
Frequency Sweep	92.5 to 97.5 MHz (Sawtooth)
Sweep Time	800 μs
Intermediate Frequency	352.5–357.5 MHz
Power Output Without Amplifier	−6.81 dBm
High Power Amplifier	Stage I: 7.81 dB Stage II: 39 dB with P1dB of 40 dBm
LNA	Noise figure of 1.9 dB gain of 36 dB P1dB of 12 dBm
Noise Floor	−118 dBm dynamic range of 102 dB
ADC	16 bits, 2 MSPS

The radar features a radome that protects it from weather and dust. Analysis of the fiberglass radome, measured from 9352 MHz to 9357 MHz, shows low attenuation values from 0.76 dB to 0.98 dB, indicating stable electromagnetic properties. This establishes fiberglass as an effective material for radome construction, owing to its low dielectric constant, mechanical strength, and light weight. However, azimuth rotation measurements indicate that attenuation varies between 0.76 dB and 1.8 dB, suggesting variations in the radome's thickness.

To analyze the rainfall structure, the FMCW weather radar used a volume scanning strategy with a rotating antenna at 2 RPM, completing a 360° sweep every 0.5 minutes. The 4-minute scanning cycle included 3.5 minutes of active scanning at seven elevation angles: 0.00°, 0.76°, 2.27°, 4.54°, 7.56°, 11.34°, and 15.88°.

2.2. Transmitter and Receiver Unit

Figure 2 presents the architectural block diagram of the transmitter and receiver components, while Table 1 details their key specifications. The transmitter subsystem comprises an AD9956 Direct Digital Synthesizer (DDS), a 450 MHz intermediate frequency (IF) signal oscillator, a 9 GHz carrier signal oscillator, and a high-power amplifier with a gain of 44.81 dB. FMCW modulation is implemented at the baseband utilizing an AD9956 evaluation board, which integrates a DDS and phase-locked loop (PLL) circuitry. The waveform generator operates with a 375 MHz reference clock, enabling a frequency sweep from 92.5 MHz to 97.5 MHz over a sweep time of 0.8 ms.

A photograph of the AD9956 Direct Digital Synthesizer (DDS) board, which is a key component of the transmitter hardware, is presented in Fig. 3(a). The generated chirp signal, depicted in Fig. 4(a), exhibits a frequency span ranging from 92.7 MHz to 97.7 MHz and an output magnitude varying from −55.2 dBm to −52.6 dBm. The measured DDS output demonstrates a highly linear frequency sweep from approximately 92.5 MHz to 97.5 MHz, yielding a chirp bandwidth of 5 MHz and a corresponding range resolution of 30 m. This linear fit, highlighted by the red line in Fig. 4(a), shows excellent correspondence with the measured data, exhibiting minimal deviation within ±0.15 dB and centered around 0 dB. This outcome

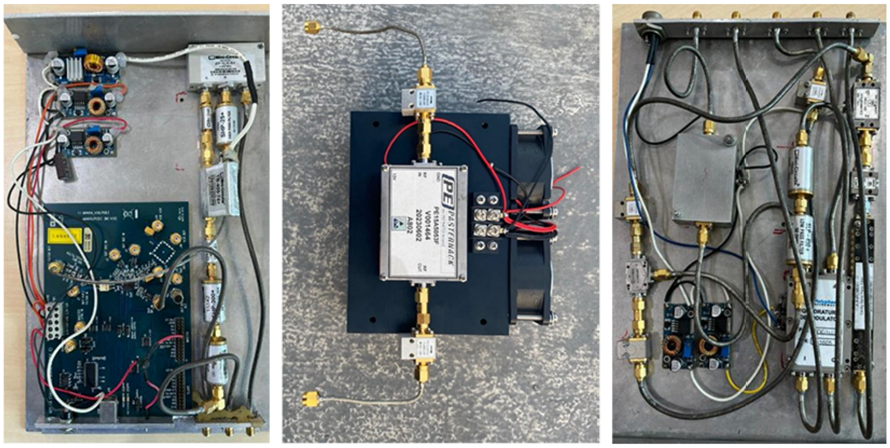
(a) (b) (c)

FIGURE 3. Photograph of the developed (a) DDS AD9956 board used for generating a chirp signal at the transmitter. (b) A high-power amplifier (HPA) with a gain of 39 dB and a 1 dB compression point at 40 dBm. (c) A quadrature demodulator designed to extract the in-phase and quadrature signals from the beat signal in the receiver system.

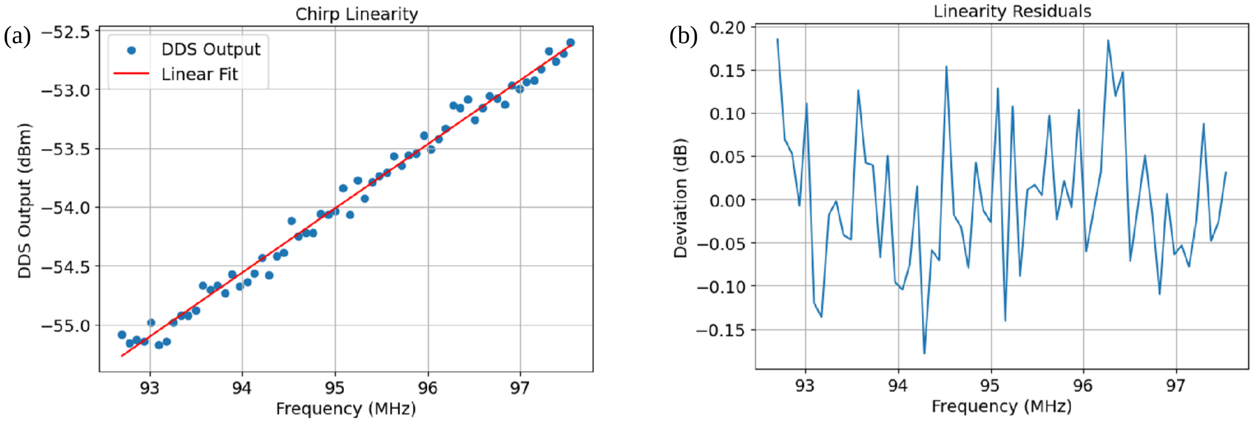

FIGURE 4. Analysis of the chirp signal generated by DDS AD9956, showing (a) the linearity of the chirp signal, with a linearity coefficient of 0.9889, and (b) the linear residuals of the chirp signal.

indicates low residual nonlinearity, the absence of systematic bias or drift, and only minor high-frequency fluctuations.

The analysis of the DDS output reveals a systematic amplitude slope of approximately 2.5 dB across the 5 MHz bandwidth (Fig. 4(a)) and quasi-periodic amplitude ripples with a peak deviation of ± 0.18 dB (Fig. 4(b)). While the 2.5 dB slope represents a linear amplitude taper, the second-stage High Power Amplifier (HPA), operating near saturation (P1dB), effectively compresses this variation, stabilizing the mean transmit power P_t used for reflectivity calibration. The primary concern regarding signal purity is the impact of the amplitude residuals (ripple) on the Range Sidelobe Level (RSL). In FMCW processing, frequency-domain amplitude ripples produce paired echoes (sidelobes) in the range profile [3]. Using the small-ripple approximation, the theoretical degradation in RSL due to the amplitude ripple of ΔA_{dB} can be estimated as [3]:

$$\mathrm{RSL}_{dB} \approx 20\log_{10}\left(\frac{10^{\frac{\Delta A_{dB}}{20}}-1}{2}\right) \tag{1}$$

Substituting the measured maximum residual of $\Delta A_{dB} \approx 0.18$ dB into Eq. (1) yields a theoretical RSL contribution of approximately -39.6 dB. This hardware-induced sidelobe floor aligns with the windowing functions used in digital signal processing (DSP), specifically the Blackman window, which produces a sidelobe suppression of about -46 dB. This level is sufficient for meteorological observations, as it prevents ghost echoes from strong clutter from significantly contaminating adjacent range bins in stratiform precipitation environments. Furthermore, since Z_e is logarithmically derived, the ± 0.18 dB source uncertainty translates to a negligible reflectivity error of < 0.2 dBz, well within the standard calibration tolerance of ± 1.0 dBz [18].

The DDS output signal undergoes a preliminary up-conversion via a double-balanced passive mixer. This mixer is driven by a local oscillator (LO) operating at 450 MHz with a power level of -14.237 dBm. This stage generates an IF chirp signal spanning from 352.5 MHz to 357.5 MHz. The IF stage incorporates amplification to compensate for the mixer's conversion loss and elevate the signal level to an appropriate magnitude for subsequent processing and eventual up-conversion to the RF. Specifically, it amplifies the DDS output, which is around -53 dBm, to an IF output power of -34 dBm. The output of this first up-conversion stage is then fed into a bandpass filter (BPF) with a bandwidth of 340 MHz to 370 MHz, effectively suppressing image frequencies and inter-modulation products. The filtered output is subsequently divided by a two-way power splitter, with one path directed to the second up-conversion stage within the transmitter and the other feeding the down-conversion stage in the receiver.

The second up-conversion employs another double-balanced mixer, driven by a low-phase-noise, phase-locked dielectric resonator LO operating at 9 GHz. The LO output power is 9.462 dBm, and this signal is split to drive both the transmitter's upconverter and the receiver's first downconverter. The mixer's output is an RF signal centered at 9355 MHz with a 5 MHz bandwidth. Owing to the inherent conversion loss introduced by the mixer, this stage includes a pre-amplification circuit positioned after the up-conversion. This pre-amplifier boosts the power of the RF signal to -6.81 dBm, which is sufficient to drive the subsequent HPA. Following this up-conversion, two stages of power amplification are implemented using HPAs. The first HPA stage amplifies the signal from -6.81 dBm to 1 dBm, providing an amplification of 7.81 dB. The second stage utilizes a 39 dB HPA, characterized by a 1 dB compression point at 40 dBm and a maximum input power handling capability of 11 dBm, which further amplifies the signal from 1 dBm to 40 dBm. A photograph of the 39 dB HPA is shown in Fig. 3(b).

The measured output power characteristics of Stage I and Stage II amplification show that Stage I consistently exhibits a low output power, measuring approximately 1 dBm, whereas Stage II maintains a nearly constant output of approximately 40 dBm across the entire input power range. The gain for Stage I is approximately 7.81 dB, remaining highly consistent and operating well within its linear region. When considering all stages together, the system achieves an overall gain of approximately 46.8 dB, highlighting its linear response across the operational input range.

In the receiver architecture, the signal path includes several key components: a Low Noise Amplifier (LNA), a mixer that works with a 9 GHz input, another mixer for a 450 MHz input, a quadrature demodulator, an Analog-to-Digital Converter (ADC), and a Signal Processing Unit (SPU). The LNA has a noise figure of 1.9 dB and a gain of 36 dB. Its output power at the 1 dB compression point is 12 dBm. To better understand the radar's noise floor and improve the data analysis, we perform a detailed examination of the LNA's characteristics. The noise floor, which represents the smallest signal that the LNA can detect, is essential for the radar sensitivity. With the LNA's gain of 36 dB and an output noise level of -82 dBm, we calculate the input noise floor by subtracting the gain from the output noise. This gives us a noise floor of -118 dBm, showing the lowest signal power that the receiver can detect above its own noise.

Beyond the noise floor, we can derive additional important performance metrics from LNA specifications. The output's 1 dB compression point (P1dB) is 20 dBm. Considering the LNA's gain, the corresponding input P1dB is -16 dBm. This means that the maximum signal power the radar can process, before the gain drops by 1 dB due to non-linearity, is -16 dBm, indicating the beginning of saturation. We also calculate the receiver's dynamic range, which is the difference between the strongest signal it can handle without distortion and the weakest detectable signal. This gives us a dynamic range of 102 dB. This wide dynamic range proves the receiver's ability to accurately process a range of signal strengths, from faint echoes to strong returns, without losing signal quality. While the noise figure of 1.9 dB provides a preliminary view of the LNA's noise contribution, a complete evaluation of the system sensitivity should also consider the receiver's operating bandwidth to determine the absolute thermal noise limit.

Following amplification by the LNA and passage through a BPF, the signal undergoes its first down-conversion from 9355 MHz to 355 MHz. This conversion is performed by a mixer identical to that employed in the transmitter's second up-conversion stage. The penultimate stage before digitalization is quadrature demodulation. A quadrature demodulator, as depicted in Fig. 3(c), is utilized to extract the in-phase (I) and quadrature (Q) components from the beat signal. These components represent the real and imaginary parts of the baseband signal, respectively, enabling the recovery of the original information. Specifically, the received signal is mixed with two versions of the transmitted chirp signal at the baseband, exhibiting a 90° phase difference, to yield the I and Q components of the beat signal. Both quadrature demodulation outputs are approximately -40 dBm, with a noise figure (NF) of -74.5 dBm. Figs. 5(a) and (b) illustrate that the two 90° phase-shifted versions of the transmitted chirp signal at the baseband possess a frequency range similar to the DDS output, albeit with a higher magnitude attributable to amplification. The analysis of the Q channel in Fig. 5(a) reveals that spurious tones and harmonics contribute to phase jitter and amplitude instability, resulting in quadrature phase error; however, the spectral envelope indicates high purity of the I/Q demodulated signal, which enhances target discrimination and dynamic range. Fig. 5(b) shows a moderate I/Q imbalance, with the Q channel displaying stronger amplitude fluctuations compared to the flatter I channel, although minor phase distortion from this imbalance can be addressed using DSP techniques. The measured signal-to-noise ratios (SNR) and amplitude stability are noted as 5.16 dB and -3.58 dB for the I channel, and 9.58 dB and -9.07 dB for the Q channel. Additionally, Fig. 5(c) illustrates a phase difference plot between the I and Q inputs, showcasing an oscillatory pattern with variations between 30° and 90°, indicating imperfections from amplitude and phase imbalance, DC offsets, and mismatched delays, which particularly impact performance in the 94.5–96.5 MHz range.

2.3. Signal Processing Unit

Equation (3) shows how the beat frequency (f_b) relates to range (R). In this equation, BW stands for bandwidth, c is the speed of light, and τ is the sweep time of the chirp [18]. Using a 16-bit ADC that samples at 2 MSPS, we can calculate the maximum

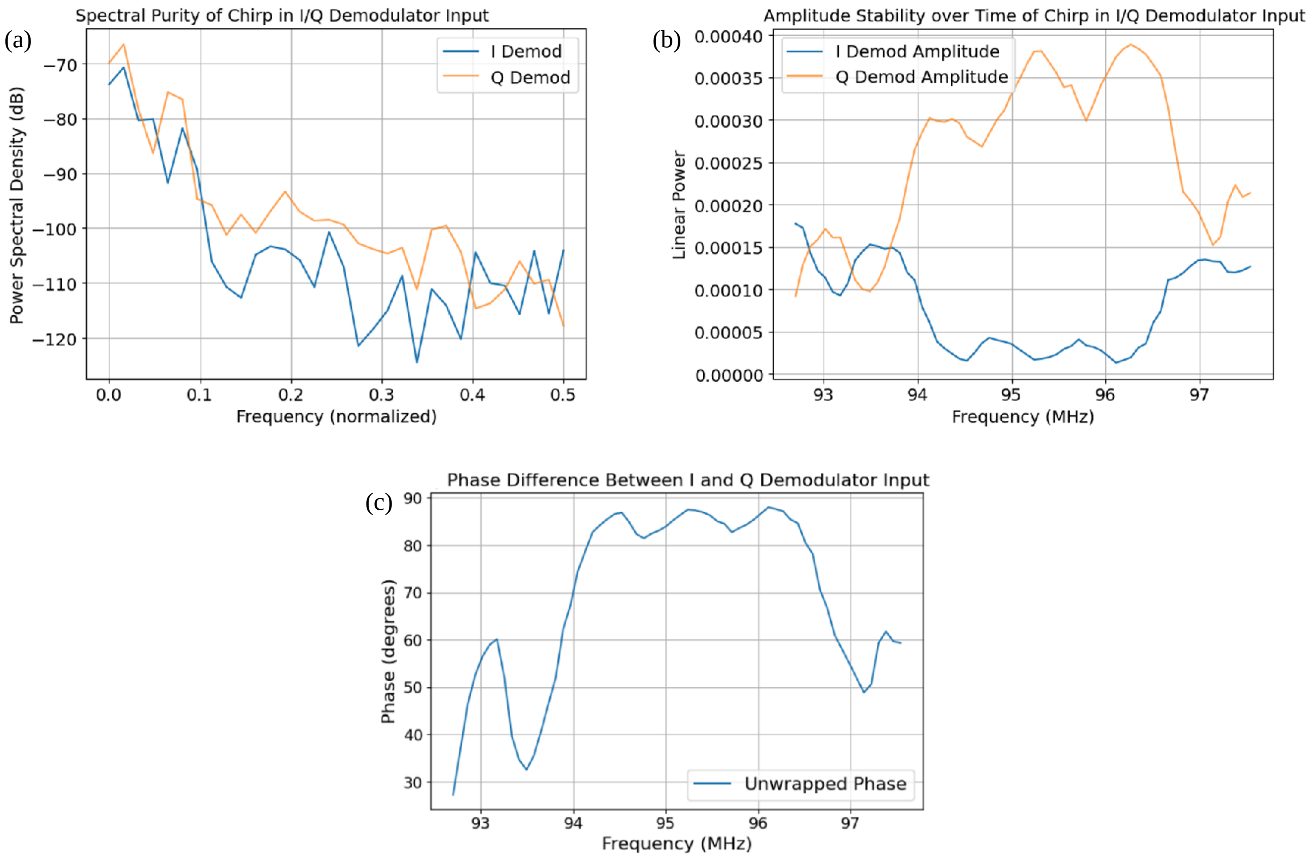

FIGURE 5. Analysis of the chirp signals in the receiver. (a) Spectral purity of chirp signal in I/Q demodulator input (FFT estimate). (b) Amplitude stability over time of chirp signal in I/Q demodulator input. (c) Phase difference between the I and Q inputs of the demodulator.

unambiguous range to be 24 kilometers when the bandwidth is 5 MHz and the sweep time is 0.8 ms. For a maximum range (R_{max}) of 15.36 km, which is 64% of the maximum unambiguous range, the beat frequency (f_b) is 640 kHz.

To suppress RSL that would otherwise mask weak meteorological echoes near strong ground clutter, a Blackman window is applied to the time-domain data prior to the FFT. While this windowing broadens the main lobe slightly (reducing pure range resolution), it provides a theoretical peak sidelobe level of approximately -46 dB, which matches the dynamic range requirements for observing precipitation gradients and ensures that the system performance is limited by hardware linearity rather than processing artifacts.

In this setup, we capture 1,600 samples per chirp, calculated as 2×10^6 samples per second $\times 0.0008$ seconds. We collect 1,600 samples for the $I(t)$ signal and another 1,600 samples for the $(Q(t)$ signal since they are sampled at the same time. To make processing easier, we use an FFT size that is a power of two. The next highest power of two after 1,600 is 2048 (2^{11}). We achieve this by adding 448 zeros to the 1,600-sample data vector. This technique, called zero-padding, allows us to perform the 2048-point FFT effectively.

$$R_{\text{max}} = \frac{f_s c \tau}{4BW} \tag{2}$$

$$f_b = \frac{2RBW}{c\tau} \tag{3}$$

$$\mathcal{Y} = \cos\xi + \sin\xi = e^{j\xi} \tag{4}$$

In the digital domain, the in-phase and quadrature remaining signals are complexly added, resulting in Eq. (4), where $\xi = \alpha - \beta = 2\pi f_b t$ is the phase difference between the transmitted and the received signals, respectively. The result of the quadrature demodulation is a complex signal. A moving target will exhibit a distinct phase shift from chirp to chirp, allowing Doppler estimation in the second FFT dimension [18].

For a weather radar operating at 9.355 GHz with a pulse repetition time (PRT) of 0.8 ms (PRF $= 1250$ Hz), the unambiguous Doppler velocity range is determined by the Nyquist velocity, given by

$$v_{\text{max}} = \pm\frac{\text{PRF} \cdot c}{4f_0}.$$

Substituting the parameters yields $v_{\text{max}} \approx \pm 10.02$ m/s, indicating that velocities between -10.02 m/s and $+10.02$ m/s can be measured without ambiguity. In contrast, the spectral width, representing the variability of velocities within the radar volume due to turbulence and shear, is a measured atmospheric property and is not limited by the radar hardware.

Stationary targets, such as terrain and buildings, produce strong echoes near zero Doppler frequency (ground clutter), which can obscure weather signals. To suppress this contamination, a high-pass filter (ground clutter filter) is applied in the Doppler processor to attenuate frequencies below a thresh-


(a) (b) (c)

FIGURE 6. Photograph of developed FMCW radar, (a) without radome, (b) with bottom side of radome, (c) with full radome.

old corresponding to minimal atmospheric motion. For a minimum velocity threshold of 0.5 m/s, the cutoff frequency is given by [18]

$$f_d = \frac{2vf_0}{c},$$

resulting in $f_d \approx 31$ Hz. Thus, implementing a high-pass filter with a cutoff near 31 Hz effectively separates weather echoes from stationary ground returns.

2.4. Radar Reflectivity Factor

Estimating the equivalent reflectivity factor (Z_e) is essential for quantifying the precipitation intensity. The enclosed formulation outlines the mathematical derivation of Z_e from the received radar power, incorporating the system parameters and physical constants. Z_e which is directly related to the radar-observed backscatter from hydrometeors (e.g., raindrops or snowflakes), is expressed as [18]:

$$Z_e(r) = C(P_r(r) - P_n)\frac{L^2_{atm}(r)}{|K_\omega|^2} \tag{5}$$

$$C = \frac{\lambda^2 512 \ln 2 \cdot 10^{18}}{P_t G_t G_{rec} \Delta r \theta_t^2 |K_\omega|^2 \pi^3} \tag{6}$$

where C is the radar calibration constant; $|K_\omega|^2$ is the dielectric factor of water; θ is the minimum between the transmitter antenna half-power beamwidth θ_t and the receiver antenna half-power beamwidth θ_r; Δr is the range resolution of the radar; G_t is the gain of the transmitting antenna; G_r is the gain of the receiving antenna; G_{rec} is the receiver chain gain; and L_{atm} is the losses due to the propagation in the atmosphere at distance r.

By using P_t of 40 dBm, G_t and G_r are 32.8 dBi, G_{rec} is 36 dB; Δr is 30 m; θ_t and θ_r are 4 degrees; $|K_\omega|^2$ is 0.93; λ is 0.03204623; and C is 260475.45. This calibration factor enables the direct conversion of the received power measurements into physically meaningful reflectivity values (expressed in mm^6/m^3 or dBz), which is essential for quantitative precipitation estimation (QPE) [19] and meteorological analysis.

2.5. Radar Tested

The developed radar operates with a rapid 4-minute volume scan across seven elevation angles (0.00° to 15.88°) and a 2 RPM antenna rotation, facilitating a complete azimuthal sweep every 0.5 minutes. Photographs of the developed radar are depicted in Fig. 6. Compared to other radar systems, such as the MP-X Radar [9] with an 11-elevation scan in approximately 3 minutes and the BoXPol Radar [10] which balances high spatial resolution with a 5-minute scan cycle across 10 elevations, this FMCW WR provides commendable temporal resolution. Although it is not as rapid as the 20-second scanning capabilities of the RaXPol [2], designed for fast-evolving phenomena, it exceeds the FMCW IDRA without volume scanning [12], which typically operates with a fixed low elevation for drizzle studies. With a power output of 10 W and a maximum range of 15 km, the radar excels in localized, high-resolution observations of shallow to moderate stratiform rain, isolated convective cells, and topographically induced convection, which are particularly relevant in complex terrain regions. The radar's capabilities significantly contribute to urban hydrology, short-term nowcasting, and the study of convective initiation [20].

The FMCW radar was set up on the rooftop of a three-story building in Yogyakarta, Indonesia (coordinates: 7.7928818° S, 110.3883323° E). On April 16, 2025, at 14:30 local time, the radar detected the rainfall while scanning the area. The results were compared and calibrated with data from the C-band pulsed Doppler WR (CDWR), located at 7.7317947° S and 110.3533411° E. The two radars are 7.8 kilometers apart, and the FMCW WR is positioned at an angle of 151.6° relative to the CDWR.

A comparison of FMCW WR and CDWR shows that each has strengths for rainfall observation. FMCW WR can detect small rainfall features because it has finer range resolution (30 m). CDWR, with its narrower beam (0.95° vs. 4°), gives better angular resolution, which helps map the shape of storms and rain areas over wide regions.

2.6. Three Stages PIML-Based Data Calibration

This study develops a multi-stage ML calibration framework to harmonize target and reference radar reflectivity mea-

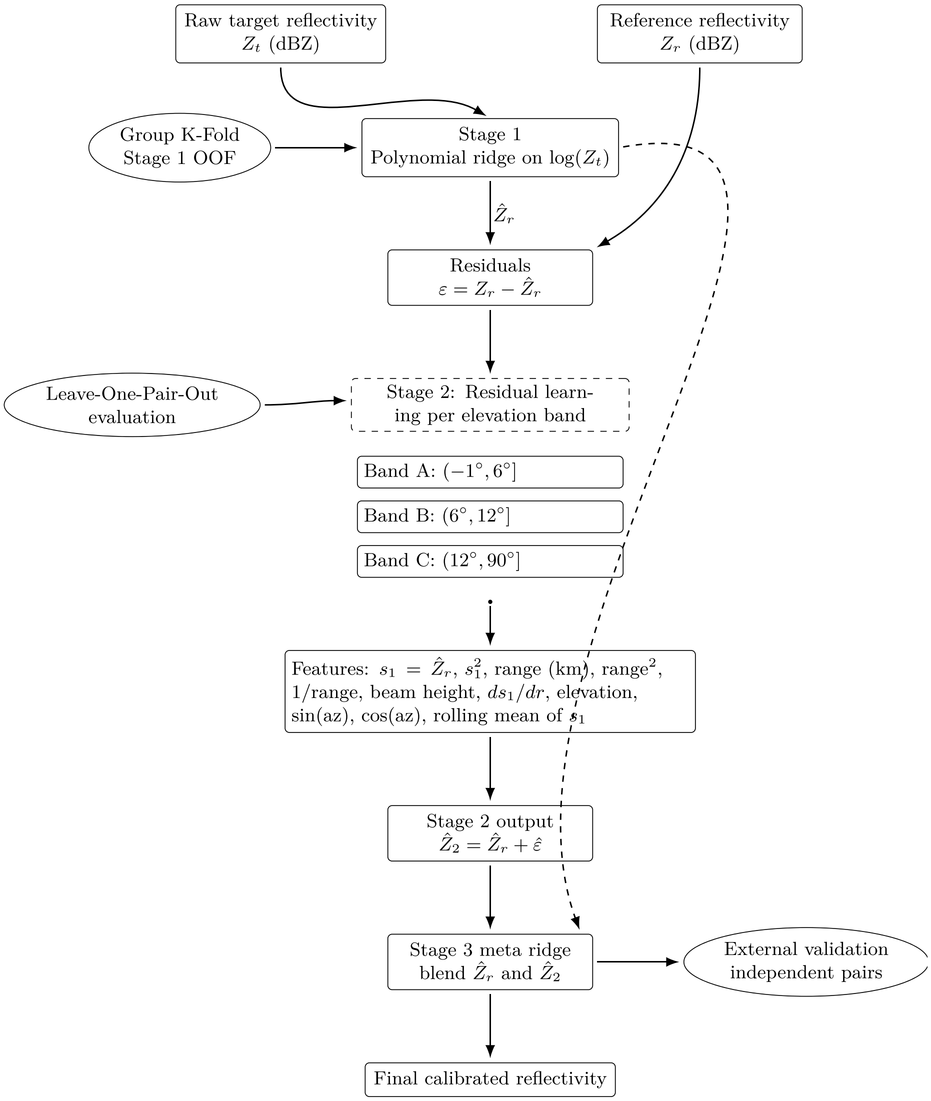

FIGURE 7. Conceptual schematic of the radar reflectivity calibration framework in vertical layout. Raw target reflectivity is mapped to a Stage 1 estimate of reference reflectivity using polynomial ridge regression on logarithmic intensity. Residuals between Stage 1 prediction and the reference are modeled in Stage 2 using band-specific gradient boosting with physically informed features that capture range dependence, beam geometry, and local gradients. Stage 3 performs meta-level ridge refinement to blend Stage 1 and Stage 2 outputs for smooth transitions across elevation bands. Validation consists of internal Group K-Fold for Stage 1, Leave-One-Pair-Out across radar pairs, and external validation using independent pairs.

surements, as illustrated in Fig. 7. The approach integrates physically guided preprocessing with data-driven models in three consecutive stages, namely Stage 1 for bias correction, Stage 2 for residual correction, and Stage 3 for meta refinement. Each stage incrementally reduces systematic and geometry-dependent errors while preserving the physical relationship among range, elevation, and radar reflectivity.

Six paired volumetric radar scans acquired on 16 April 2025 were used for model development, covering elevation angles from $0.5°$ to $14.6°$. Each target radar dataset was collocated with its corresponding reference radar sweep at identical azimuth range grids. Quality control was applied by retaining only samples with reflectivity between 25 and 65 dBz for both target and reference data, which removed spurious noise and saturation artifacts.

Stage 1 performs baseline calibration between the target and reference reflectivity using a ridge-regularized polynomial regression on log-transformed intensities. The model approximates the reference reflectivity $\hat{Z}_r$ as a function of $\log(Z_t)$ expanded up to the second-order polynomial. This stage primarily captures global biases and mild nonlinearities in the receiver response. The validation of Stage 1 employed a five-fold Group K-Fold cross-validation strategy, where all samples from a single radar pair were withheld together in each fold. The resulting out-of-fold (OOF) predictions provided unbiased residuals for Stage 2 training.

Stage 2 models the spatially varying residuals between the reference and Stage 1 predictions as a function of the radar-geometry variables. The residuals were defined as $\varepsilon = Z_r - \hat{Z}_r$ and standardized per radar pair before training. The modeling used XGBoost regressors with squared-error objective, 1500 trees, a learning rate of 0.02, a maximum tree depth of 2, a minimum child weight of 8, and regularization parameters $\lambda = 2.0$ and $\alpha = 1.0$ [21]. Residuals were modeled separately within elevation bands defined as $(-1°,\ 6°)$, $(6°,\ 12°)$, $(12°,\ 90°)$. Bands containing fewer than 6000 samples were automatically merged with adjacent ones to ensure sample sufficiency. Each band model included an internal validation subset for early stopping.

Stage 2 employed a set of physically meaningful predictors representing radar geometry and signal propagation. The feature vector **x** included the Stage 1 calibrated reflectivity $\hat{Z}_r$ and its square $\hat{Z}_r^2$, ranging in kilometers r_{km} together with its inverse r_{km}^{-1} and square r_{km}^2, beam height h_b computed under the four-thirds Earth approximation, finite-difference range gradient of reflectivity $\frac{\partial \hat{Z}_r}{\partial r}$, elevation angle θ_{elev}, azimuthal sine and cosine components $\sin(\phi_{az})$ and $\cos(\phi_{az})$, and five-point rolling mean of the Stage 1 reflectivity $\overline{\hat{Z}_r}^{(5)}$. These radar geometry and elevation-dependent effects were explicitly modeled, following the emerging use of ML correction of radar-derived reflectivity fields [22]. The beam height h_b was calculated using the four-thirds Earth approximation as follows:

$$h_b = \sqrt{r^2 + (kR_e)^2 + 2rkR_e \sin\theta_e} - kR_e \tag{7}$$

where r is the slant range from the radar (m), R_e the mean Earth radius (6,371,000 m), k the effective Earth-radius factor (commonly $4/3$ to account for standard atmospheric refraction), and θ_e the radar beam elevation angle (degrees or radians). This formulation accounts for Earth curvature and atmospheric bending, providing the geometric height of the radar beam center above the radar antenna [18].

Such corrections have been shown to be important in modern radar calibration workflows [23], as they improve the accuracy and consistency of radar-derived reflectivity fields, especially when dealing with variable propagation conditions across different elevation angles.

These features capture the nonlinear dependence of reflectivity errors on the range, elevation, and beam geometry. All features were standardized prior to training. The predicted residuals were added to the Stage 1 predictions to yield the Stage 2 calibrated reflectivity field.

Stage 3 provides meta-level refinement by blending the outputs of Stage 1 and Stage 2 through a ridge regression model. The meta features consisted of Stage 1 and Stage 2 predictions, their squares, beam height, range, and elevation. This stage enforces smooth transitions between the elevation bands and prevents local overcorrection. The ridge regularization coefficient was fixed at $\alpha = 1.5$.

The complete validation scheme comprised four hierarchical levels. Stage 1 was validated internally through a 5-fold Group K-Fold cross-validation scheme, where each subset of radar pairs served once as the validation group while the remaining subsets were used for training. Stage 2 employed the inner training and validation subsets for early stopping. The overall framework was evaluated using a LOPO scheme, where one radar pair was excluded entirely for testing in each fold [24]. Finally, a separate external validation experiment was conducted using six independent radar pairs at 14:27 LT to evaluate the generalization to the unseen data. For production readiness, a model was trained using all internal pairs combined. The mean squared error (MSE) between predicted and reference reflectivity was used as the primary performance metric.

3. RESULTS AND DISCUSSION

3.1. Calibration Results

The cross-validation results demonstrate that the proposed calibration framework significantly improves the consistency and accuracy of radar reflectivity relative to the reference measurements. Across the six internal radar pairs, Stage 1 produced an average MSE of 388 dBz^2. Stage 2 reduced this error to 308 dBz^2, representing an average improvement of 80 dBz^2. Stage 3 achieved a final mean MSE of 310 dBz^2, confirming that the meta-regression effectively stabilized the calibration without loss of accuracy. Table 2 summarizes the detailed results for each radar pair in the LOPO evaluation.

TABLE 2. LOPO cross-validation results in MSE.

Pair ID	S1	S2	S3	Δ_{12}	Δ_{13}
00	336.0	328.8	298.5	+7.2	+37.5
01	346.3	338.1	295.4	+8.2	+50.9
02	350.7	218.6	217.0	+132.0	+133.6
03	454.5	341.4	352.6	+113.1	+101.9
04	445.6	287.6	291.1	+157.9	+154.5
05	395.5	330.9	406.1	+64.6	−10.5
Mean	388.1	307.6	310.1	+80.5	+78.0

All pairs improved, except for the highest-elevation pair (pair 05). For pair 05, which usually has strong signal loss and small overlap, the error stayed steady instead of getting worse. This shows that band-wise residual learning and meta-regularization helped prevent overfitting at high elevation angles.

Combining all internal pairs for training, Stage 1 had a mean squared error (MSE) of 372.2 dBz. Stage 2 improved to 182.2 dBz, and Stage 3 reached 178.0 dBz. It means that the error variance dropped by 52%, and the root mean square error fell by about 30% (from 19.3 to 13.3 dBz). Using the same model on six external radar pairs gave almost the same results: Stage 1 MSE $=$ 372.6, Stage 2 $=$ 186.1, Stage 3 $=$ 182.7 dBz. A comparison is presented in Table 3.

TABLE 3. Performance of the calibration system measured in MSE on internal and external datasets.

Evaluation Set	S1	S2	S3	Δ_{12}	Δ_{13}
Internal (All)	372.2	182.2	178.0	+190.0	+194.2
External	372.6	186.1	182.7	+186.5	+189.9

The internal and external results are nearly identical, showing that the calibration model works well on new data without losing accuracy. Both validation levels show a consistent 50%

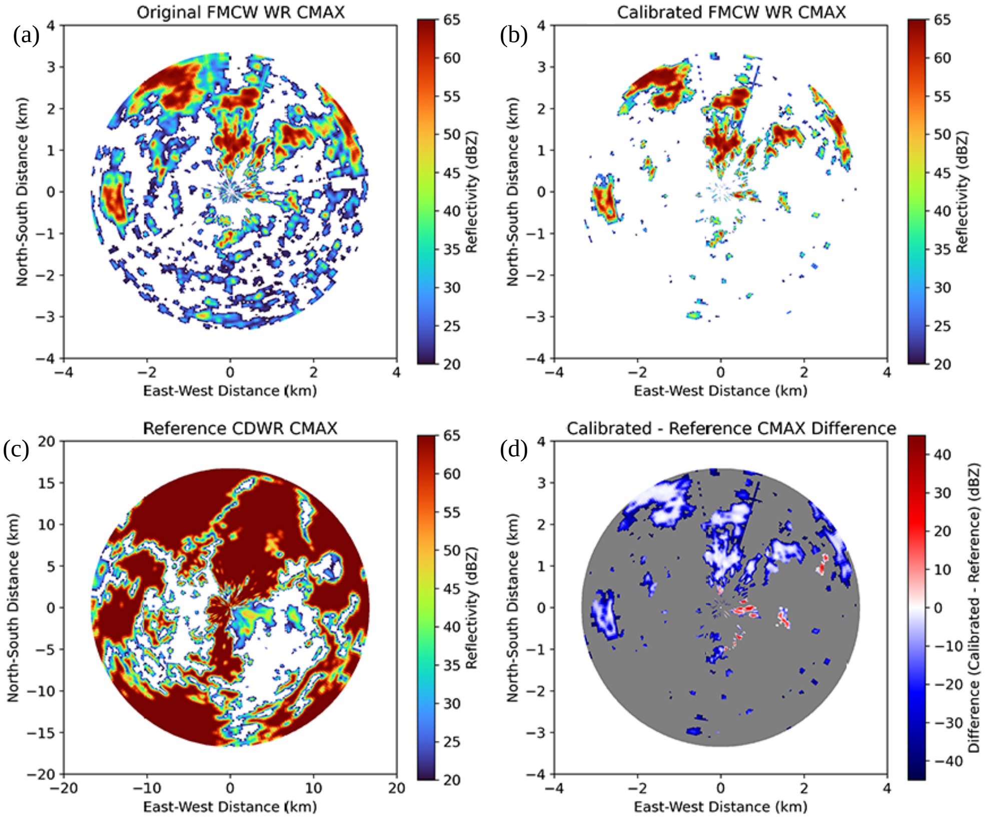

FIGURE 8. Comparison of CMAX between the original and calibrated results of FMCW WR, along with the reference CDWR, and the difference between calibrated FMCW WR and CDWR. The rainfall observation occurred on April 16, 2025, at 14:30 LT.

drop in MSE, meaning that the model corrects instrument bias and accounts for the effects of propagation and attenuation.

Adding physical parameters like beam height, range gradient, and elevation angle made the model easier to understand and improved its performance. The meta-stack refinement helped keep results consistent across elevation bands, which is important for radar and rainfall estimates. Most errors at high elevation angles are due to fewer samples and more noise. Future improvements could include better attenuation correction or smoothing over time.

The analysis reveals that the model relies most heavily on geometric and spatial features rather than the reflectivity magnitude itself. The azimuthal components $\sin(\phi_{az})$ and $\cos(\phi_{az})$ exhibit the highest importance scores. This pronounced azimuthal dependency suggests that the residual errors are spatially anisotropic, likely stemming from sector-specific beam blockage, partial beam filling, or orientation-dependent interference patterns inherent to the radar's deployment environment.

Figure 8 shows CMAX from the original data, the calibrated FMCW WR, the reference CDWR, and the difference between the calibrated FMCW and the reference. In the original FMCW CMAX, reflectivity is scattered with large low-reflectivity areas (below 35 dBz) and a few strong cores. This means that the original FMCW underestimates rainfall and misses continuous rain structures, mainly due to rainfall attenuation and a wide scanning beam. After calibration, the CMAX field looks more like typical rainfall, showing higher reflectivity and clearer rain cores. The calibrated FMCW reflectivity increases in key areas, matching the reference data better.

The reference CDWR CMAX (Fig. 8(c)) shows large, continuous areas of high reflectivity (over 45 dBz), meaning strong, organized rainfall. The reference radar covers more area than the calibrated FMCW because it is more sensitive and has a wider range.

The difference between the calibrated FMCW and reference CMAX (Fig. 8(d)) shows that some differences remain after calibration. Calibration reduces most of the bias, but some areas still have higher values (> 10 dBz), where the FMCW measures more reflectivity than the reference. Other areas have lower values (< -10 dBz), meaning that the FMCW underestimates reflectivity. These remaining differences are found in specific places and may be due to calibration limits, different beam shapes, or mismatches in how the two systems sample the rain.

Figure 9 shows Range Height Indicator (RHI) plots of reflectivity at about $151.6°$ and $208.4°$ from the CDWR and the FMCW WR. The azimuth slices match FMCW WR's position relative to the CDWR. These plots show a vertical cross-section of the rain, making it possible to see how rainfall is distributed and how intense it is along those directions.

The CDWR RHI (Fig. 9(a)) shows a tall, deep area of rain, with reflectivity higher than 50 dBz near the ground and above 30 dBz up to 56 km high. This means that there is strong, tall, and heavy rainfall, which is typical of mature storm cells. The rain is widespread and continuous, showing a large, organized

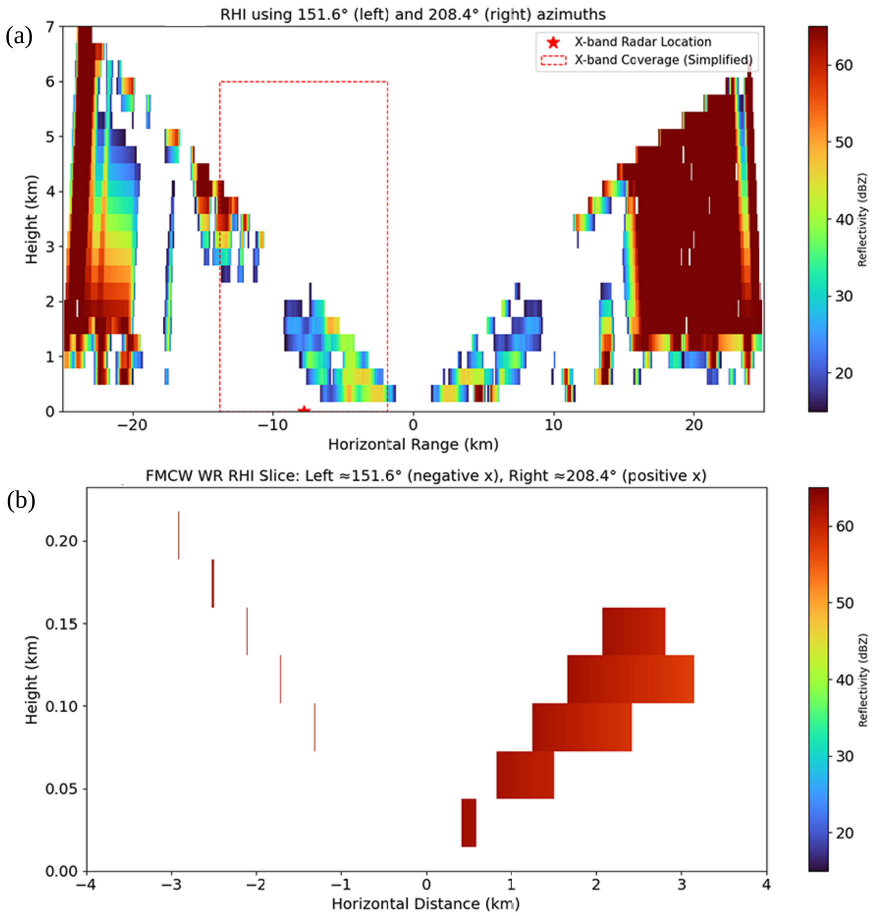

FIGURE 9. RHI plot at azimuth angles of 151.6° and 208.4° for (a) CDWR and (b) FMCW WR. The rainfall observation was recorded on April 16, 2025, at 14:30 LT.

storm. The strongest rain is near the ground but extends high up, matching the pattern of heavy rain reaching the surface.

In contrast, the FMCW WR RHI (Fig. 9(b)) shows much shallower and more local rain signals. The echoes only go up to about 200 m high and cover a small area. The reflectivity is still high (over 50 dBz) near the ground, showing strong rainfall, but the vertical range is limited because the FMCW radar cannot see as far. This means that the FMCW radar is good at seeing fine details of rain near the surface, but cannot capture the full height of the storm like the CDWR.

The calibration was checked by comparing the original and calibrated reflectivity with the reference data (see Table 4). The comparison used root mean square error (RMSE) and bias. Only reflectivity values between [20, 65] dBz were used, focusing on real rain signals. This range is based on the standard rainfall reflectivity [25].

TABLE 4. Comparison of reflectivity metrics for original (Ori) and calibrated (Cal) datasets relative to the reference.

Metric	Elevation (°)				
	0.76	**2.27**	**4.54**	**7.56**	**15.88**
RMSE (Ori)	30.24	29.92	37.04	42.58	13.41
Bias (Ori)	−27.38	−26.75	−35.94	−42.58	−7.19
RMSE (Cal)	10.11	11.88	8.37	5.07	29.79
Bias (Cal)	−2.37	1.13	0.62	−5.06	28.39

Table 4 summarizes the RMSE and bias of the original and calibrated reflectivity across different elevation angles. The calibrated reflectivity shows significant improvements in both RMSE and Bias, particularly at lower and mid-level elevations. For instance, at 7.56°, RMSE dropped from 42.58 dBz to 5.07 dBz, and Bias from −42.58 dBz to −5.06 dBz; at 4.54°, RMSE decreased from 37.04 dBz to 8.37 dBz. At 15.88°, however, RMSE increased to 29.79 dBz. This slight increase is likely not due to overfitting but rather due to a combination of factors such as reduced sample size and increased measurement uncertainty at higher elevations. While Stage 3 of the calibration framework effectively regularizes and refines residuals, the lower signal strength at higher angles may lead to greater uncertainty in calibration, highlighting the challenge of working with sparser data and the difficulty of achieving the same level of accuracy as that at lower elevations.

The elevation-dependent performance shown in Table 4 reveals how the calibration accuracy varies with beam geometry and propagation effects. The largest improvement occurs at low and mid elevation angles (0.76°–7.56°), where the RMSE decreases from more than 30 dBz in the original data to below 12 dBz after calibration. These beams intersect the main precipitation core and benefit most from the three-

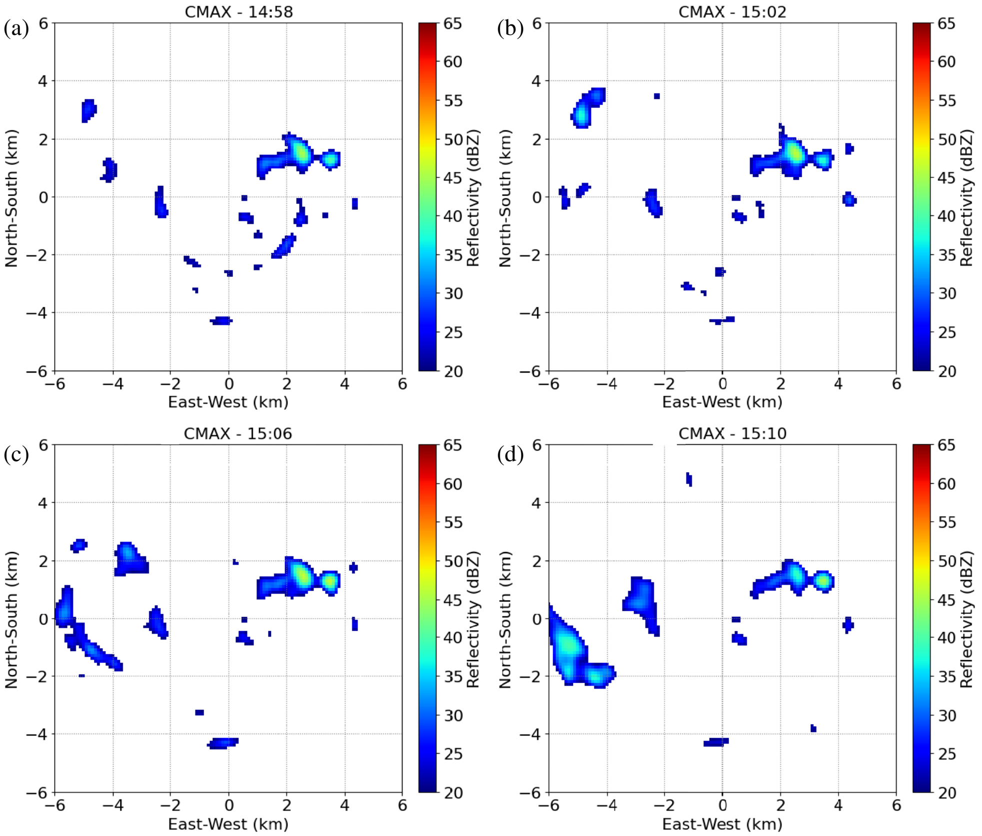

FIGURE 10. Calibrated CMAX of localized urban rainfall observed by the FMCW WR on April 12, 2025 at (a) 14:58 LT, (b) 15:02 LT, (c) 15:06, and (d) 15:10 LT.

stage correction sequence, in which Stage 1 removes the baseline bias; Stage 2 adjusts the residual range-dependent errors through band-specific learning; and Stage 3 refines the transition between elevation bands. At the lowest angles, partial beam blockage and ground clutter occasionally increase residual noise, while at the highest elevation (15.88°), the calibration performance slightly degrades due to reduced overlap with the C-band reference volume and the smaller sample size available for model training. Overall, the results indicate that the hierarchical calibration framework effectively compensates for range- and elevation-dependent biases, yielding consistent reflectivity alignment across the full scanning volume and demonstrating the system's capability to produce CDWR-comparable quantitative measurements.

The FMCW WR's 4-minute full volume scan, which is faster than the CDWR's 4.8-minute scan cycle, offers a significant advantage for real-time monitoring of rapidly evolving rainfall and storm dynamics. In addition, the FMCW WR provides five times finer range resolution (30 m vs. 150 m), allowing it to capture small-scale rainfall features with high precision [12]. This high spatial resolution is crucial for studying localized precipitation processes, particularly in complex terrain where rainfall variability is often pronounced over short distances. Although the narrower beamwidth of the CDWR (0.95° vs. 4°) allows for superior angular resolution, the FMCW WR compensates with its rapid scan cycle, which enables high-frequency temporal sampling. This feature provides detailed insights into short-term precipitation dynamics and convective initiation, making it especially valuable for fast-changing weather patterns [26].

A three-stage PIML calibration framework was developed to ensure that the FMCW WR's high-resolution measurements match the reference CDWR data. Stage 1 uses polynomial ridge regression to correct the baseline bias in the raw FMCW reflectivity; Stage 2 introduces band-specific residual learning through gradient boosting models, accounting for range, beam geometry, and elevation; and Stage 3 applies meta-ridge refinement to stabilize transitions across elevation bands. This hierarchical approach enhances the calibration's accuracy by addressing both baseline biases and elevation-dependent errors, making it robust for real-world applications.

While traditional FMCW calibration methods, such as that proposed by Myagkov et al. [27], primarily correct reflectivity biases through a single-stage polynomial approach, our method extends this by incorporating range-dependent corrections and higher-resolution adjustments to the data. This multi-step calibration provides more precise alignment with the reference data across the full scanning volume, ensuring improved performance, particularly at higher elevations where signal strength and sample size limitations are typically challenging.

The calibration results confirm the applicability of the three-stage method for each volume scan dataset from the FMCW WR, replacing previous methods that used CDWR data without volume scanning [28].

3.2. Case Study of Localized Urban Convection

Figure 10 shows the rainfall measured by a low-power (10 W) FMCW WR, while Fig. 11 shows the data from a high-power (350 kW) CDWR. The rainfall comes from local urban storms. The CDWR, with more power and a longer wavelength, is better at detecting weak rain that the FMCW WR misses. The FMCW WR, likely at X-band or higher frequencies, is more affected by signal loss behind strong storms, so it underestimates the rain in those areas.

Radar data from April 12, 2025, between 14:58 and 15:10 LT, shows the growth of a local multi-cell storm at its strongest stage. The CMAX data shows clear, intense rain cores reaching 55–60 dBz, meaning rain rates over 50 mm/hr and likely small hail in the strongest areas. The storm evolves in two ways: the main cluster ($x \approx 2\,\text{km}$, $y \approx 1\,\text{km}$) stays strong the whole time, while scattered cells in the southwest ($x \approx -5\,\text{km}$) are combined into a larger, stronger area by 15:10. Calibrated data makes these features clearer by reducing noise, showing more continuous areas of heavy rain than the raw data.

Despite its limits, such as artifacts near the radar from system leakage and ground clutter, the FMCW WR provides much finer details and reveals small structures inside storm cells. It cannot match the CDWR's wide range or ability to detect weak rain, but calibration lets it measure strong storm cores accurately. This makes FMCW WR useful for high-resolution, local monitoring of flood-causing storms, especially in cities or complex terrain. Using data from both the FMCW WR and CDWR, along with other sensors, gives a better overall view of rainfall and helps improve the hydrological analysis in the area [11, 29].

4. CONCLUSION

This study presented the design, integration, and evaluation of a pioneering transportable X-band FMCW weather radar that introduces a fully implemented volume-scanning architecture within a compact, low-power platform. The system integrates a miniaturized RF chain, a carbon graphite antenna engineered for stable beam performance, and a dedicated real-time signal-processing unit optimized for multi-elevation FMCW operation. This configuration enables rapid seven-elevation volumetric scans with high azimuthal sampling, representing a significant advancement in the electromagnetic and system-level design of FMCW radars.

The three-stage PIML hierarchical calibration framework was implemented to ensure quantitative accuracy in the FMCW WR's measurements, using collocated CDWR observations as reference data. Validation through internal five-fold Group K-Fold cross-validation, LOPO testing, and external evaluation using independent radar pairs demonstrated the framework's robustness. The model relies most heavily on geometric and spatial features rather than the reflectivity magnitude itself. Internally, MSE decreased from approximately 372 dBz^2 after Stage 1 to 182 dBz^2 after Stage 2, and further to 178 dBz^2 after Stage 3. External validation yielded comparable results.

The case study of localized urban convection observed by the FMCW WR shows that the developed low-cost radar offers much finer range resolution and can reveal detailed structures within convective cells.

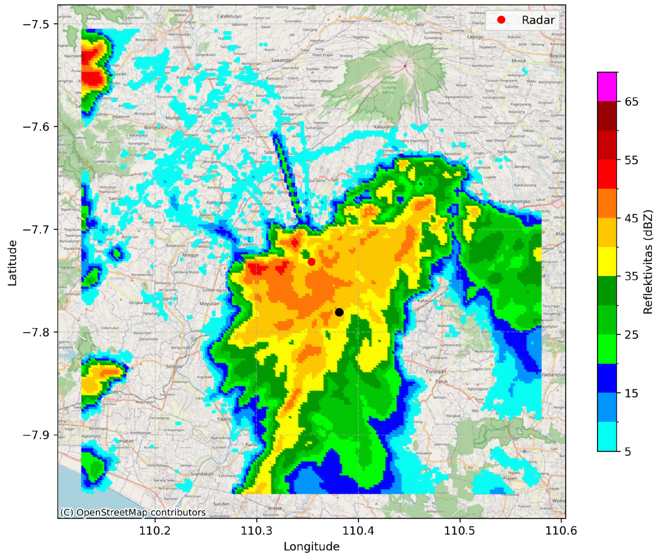

FIGURE 11. This CMAX rainfall image of CDWR running at up to 350 kW. Captured on April 12, 2025, at 15:00 LT, it shows data within a 25 km radius. The red circle marks the CDWR location, and the black circle shows the FMCW WR position.

ACKNOWLEDGEMENT

This work was funded by the Innovative Research Productive Competition of Indonesia Endowment Fund for Education Agency (LPDP), Grant Number KEP-27/LPDP/2020.

REFERENCES

[1] Antes, T., Z. Kollár, T. Zwick, and B. Nuss, "High-accuracy range estimation for FC-FMCW radar using phase evaluation in static scenarios," in *2024 IEEE Radar Conference (RadarConf24)*, 1–6, Denver, CO, USA, May 2024.

[2] Pazmany, A. L., J. B. Mead, H. B. Bluestein, J. C. Snyder, and J. B. Houser, "A mobile rapid-scanning X-band polarimetric (RaXPol) Doppler radar system," *Journal of Atmospheric and Oceanic Technology*, Vol. 30, No. 7, 1398–1413, 2013.

[3] Jankiraman, M., *FMCW Radar Design*, Artech House, 2018.

[4] Aboserwal, N., J. L. Salazar-Cerreno, and Z. Qamar, "An ultra-compact X-band dual-polarized slotted waveguide array unit cell for large E-scanning radar systems," *IEEE Access*, Vol. 8, 210 651–210 662, 2020.

[5] Uno, T., T. Uesaka, N. Nakamoto, T. Fukasawa, T. Takahashi, Y. Inasawa, T. Yamamoto, T. Koyanagi, I. Kakimoto, and Y. Konishi, "Design of a dual-polarized low sidelobe slotted waveguide antenna for C-band phased array weather radar," in *2022 IEEE International Symposium on Phased Array Systems & Technology (PAST)*, 1–4, Waltham, MA, USA, 2022.

[6] Awaludin, A., J. T. S. Sumantyo, K. Ito, S. Gao, A. Munir, M. Z. Baharuddin, and C. E. Santosa, "Equilateral triangular slot antenna for communication system and GNSS RO sensor of GAIA-I microsatellite," *IEICE Transactions on Communications*, Vol. E101-B, No. 3, 835–846, 2018.

[7] Awaludin, A., J. T. S. Sumantyo, C. E. Santosa, and M. Z. Baharuddin, "Axial ratio enhancement of equilateral triangular-ring slot antenna using coupled diagonal line slots," *Progress In Electromagnetics Research C*, Vol. 70, 99–109, 2016.

[8] Omar, M. F. M., A. A. Manaf, M. F. Ain, and S. K. A. Rahim, "A review on multi-geometrical antenna reflector," *ELEKTRIKA — Journal of Electrical Engineering*, Vol. 23, No. 3, 77–83, 2024.

[9] Park, S. G., M. Maki, K. Iwanami, V. N. Bringi, and V. Chandrasekar, "Correction of radar reflectivity and differential reflectivity for rain attenuation at X band. Part II: Evaluation and application," *Journal of Atmospheric and Oceanic Technology*, Vol. 22, No. 11, 1633–1655, 2005.

[10] Pejcic, V., J. Soderholm, K. Mühlbauer, V. Louf, and S. Trömel, "Five years calibrated observations from the University of Bonn X-band weather radar (BoXPol)," *Scientific Data*, Vol. 9, No. 1, 551, 2022.

[11] Sinatra, T., G. A. Nugroho, Halimurrahman, N. Cholianawati, A. Indrawati, F. Renggono, E. Yulihastin, S. Lestari, U. A. Ahmad, W. Widada, and A. Awaludin, "Extreme precipitation over complex terrain using multiple remote sensing observation: A case study in the Great Bandung, Indonesia," *Remote Sensing Applications: Society and Environment*, Vol. 32, 101058, 2023.

[12] Leijnse, H., R. Uijlenhoet, C. Z. Van De Beek, A. Overeem, T. Otto, C. M. H. Unal, Y. Dufournet, H. W. J. Russchenberg, J. F. i Ventura, H. K. Baltink, and I. Holleman, "Precipitation measurement at CESAR, The Netherlands," *Journal of Hydrometeorology*, Vol. 11, No. 6, 1322–1329, 2010.

[13] Salami, D., N. Bahmani, H. Yiğitler, and S. Sigg, "Adaptive internal calibration for temperature-robust mmWave FMCW radars," *arXiv:2511.02884*, 2025.

[14] Joshil, S. S. and C. V. Chandrasekar, "Calibration of D3R weather radar using UAV-hosted target," *Remote Sensing*, Vol. 14, No. 15, 3534, 2022.

[15] Jorquera, S., F. T. Bittner, J. Delanoë, A. Berne, A.-C. Billault-Roux, A. Schwarzenboeck, F. Dezitter, N. Viltard, and A. Martini, "Calibration transfer methodology for cloud radars based on ice cloud observations," *Journal of Atmospheric and Oceanic Technology*, Vol. 40, No. 7, 773–788, 2023.

[16] Bringi, V. N. and V. Chandrasekar, *Polarimetric Doppler Weather Radar: Principles and Applications*, Cambridge University Press, 2001.

[17] Shahpari, M. and D. V. Thiel, "The impact of reduced conductivity on the performance of wire antennas," *IEEE Transactions on Antennas and Propagation*, Vol. 63, No. 11, 4686–4692, 2015.

[18] Doviak, R. J. and D. S. Zrnic, *Doppler Radar & Weather Observations*, Academic Press, 2014.

[19] Sinatra, T., A. Awaludin, F. Nauval, and C. Purnomo, "Calibration of spatial rain scanner using rainfall depth of rain gauges," in *IOP Conference Series: Earth and Environmental Science*, Vol. 893, No. 1, 012064, 2021.

[20] Saadi, M., C. Furusho-Percot, A. Belleflamme, S. Trömel, S. Kollet, and R. Reinoso-Rondinel, "Comparison of three radar-based precipitation nowcasts for the extreme July 2021 flooding event in Germany," *Journal of Hydrometeorology*, Vol. 24, No. 7, 1241–1261, 2023.

[21] Wei, C.-C. and C.-C. Hsu, "Extreme gradient boosting model for rain retrieval using radar reflectivity from various elevation angles," *Remote Sensing*, Vol. 12, No. 14, 2203, 2020.

[22] Yin, Y., J. He, J. Guo, W. Song, H. Zheng, and J. Dan, "Enhancing precipitation estimation accuracy: An evaluation of traditional and machine learning approaches in rainfall predictions," *Journal of Atmospheric and Solar-Terrestrial Physics*, Vol. 255, 106175, 2024.

[23] Sanchez-Rivas, D. and M. A. Rico-Ramirez, "Calibration of radar differential reflectivity using quasi-vertical profiles," *Atmospheric Measurement Techniques*, Vol. 15, No. 2, 503–520, 2022.

[24] Yao, Y., W. D. Swaef, S. Geirnaert, and A. Bertrand, "EEG-based decoding of selective visual attention in superimposed videos," *IEEE Journal of Biomedical and Health Informatics*, Vol. 29, No. 10, 7248–7261, 2025.

[25] Oceanic, N. and A. A. (NOAA), "Jetstream: Reflectivity," https://www.noaa.gov/jetstream/reflectivity, 2023.

[26] Toledo, F., J. Delanoë, M. Haeffelin, J.-C. Dupont, S. Jorquera, and C. L. Gac, "Absolute calibration method for frequency-modulated continuous wave (FMCW) cloud radars based on corner reflectors," *Atmospheric Measurement Techniques*, Vol. 13, No. 12, 6853–6875, 2020.

[27] Myagkov, A., S. Kneifel, and T. Rose, "Evaluation of the reflectivity calibration of W-band radars based on observations in rain," *Atmospheric Measurement Techniques*, Vol. 13, No. 11, 5799–5825, 2020.

[28] Lengfeld, K., M. Clemens, C. Merker, H. Münster, and F. Ament, "A simple method for attenuation correction in local X-band radar measurements using C-band radar data," *Journal of Atmospheric and Oceanic Technology*, Vol. 33, No. 11, 2315–2329, 2016.

[29] Nugroho, G. A., Halimurrahman, A. Awaludin, I. Fathrio, N. J. Trilaksono, E. Maryadi, T. Sinatra, F. Renggono, D. Satiadi, E. Makmur, *et al.*, "A 4-years of radar-based observation of bow echo over Bandung Basin Indonesia," *Geoenvironmental Disasters*, Vol. 11, No. 1, 19, 2024.